Microporous and Mesoporous Materials 204 (2015) 62–72

Contents lists available at ScienceDirect

Microporous and Mesoporous Materials

journal homepage: www.elsevier.com/locate/micromeso

Pd-doped β-Bi_2O_3/$Bi_2Sn_2O_7$ hybrid nanocomposites for photocatalytic fluorene oxidation: A green approach for the synthesis of fluorenone/fluorenol mixture

Mohamed Mokhtar Mohamed [a,*], Saleh A. Ahmed [b]

[a] Benha University, Faculty of Science, Chemistry Department, Benha, Egypt
[b] Umm Al Qura University, Faculty of Applied Science, Chemistry Department, Makkah, Saudi Arabia

ARTICLE INFO

Article history:
Received 16 August 2014
Received in revised form 16 October 2014
Accepted 8 November 2014
Available online 15 November 2014

Keywords:
Bi oxide–Sn oxide
Heterojunction
Photocatalysis
Photo-oxidation
Fluorene

ABSTRACT

Bismuth oxide, tin oxide and Pd metal (Pd/$SnBi_{3SG}$) hybrids, synthesized via sol–gel technique while employing polyethylene glycol template at a ratio of 3 (Bi/Sn = 3) were tested toward the photocatalytic oxidation of fluorene under ultraviolet and visible light irradiations in comparison with Pd/Bi_{SG} and Pd free $SnBi_{3SG}$ photocatalysts. These catalysts were characterized using X-ray diffraction (XRD), UV–vis diffuse reflectance (DRUV–vis), N_2 sorptiometry, Raman spectroscopy, transmission electron microscopy (TEM) and GC–MS technique, which used for analyzing the photo-oxidation products. The actual photocatalyst exhibited the highest activity (100% conversion, TOF ≈ 9.4×10^{-6} s^{-1}, fluorenone/fluorenol = 3/1) following oxygen flushing for 30 min (35 ml/min) before UV irradiation. This was mainly due to the close proximity between β-Bi_2O_3 and $Bi_2Sn_2O_7$ heterojunction as well as increasing the mesoporosity margin comparatively. On the other hand, the Pd/Bi_{SG} catalyst that exhibited smaller crystallite size (20 nm vs. 44 nm) and higher surface area (21.0 vs. 12.0 m^2/g) than Pd/$SnBi_{3SG}$ indicated lower activity (Pd/Bi_{SG}, 72% conv.). This highlights the importance of the modified electronic structure of Pd/$SnBi_{3SG}$ in designing efficient charge separation as well as high quantum yield value ($\Phi \sim 0.1 \pm 0.05$) exceeding that of Pd/Bi_{SG} (3×10^{-2}) and $SnBi3_{SG}$ (10^{-2}) photocatalysts. The catalytic behavior and mechanism, reactivity–structure relationship and recyclable use of the hybrid photocatalysts have been thoroughly examined. An indirect chemical probe method using active species scavengers elucidated that the photo-oxidation mechanism was proceeded via holes and O_2^- moieties rather than singlet oxygen moieties.

1. Introduction

Fluorene, as a polycyclic aromatic hydrocarbon (PAH), is formed during the combustion of fossil fuels, such as in the oil processing plant, incomplete fuel combustion [1], asphalt transformation plants [2] and also emitted from automotive exhaust pipes [3–5]. They have a great impact on human health, most of these molecules provoking breathing diseases and cancers [6]. Fluorene is reported to possess extremely serious toxicity as well as potential mutagenic and carcinogenic properties [7]. These chemicals, which extended residence times in the environment usually enter into the atmosphere, rivers and soil through evaporation, spreading and penetration thereby causing environmental pollution. The influence of PAHs' transmission upon the nation's environmental quality and health has received extensive attention. Owing to the high toxicity of PAHs, numerous studies were performed to either degrade or remove them [8]. However, getting the maximum benefit of such high toxic compounds by performing reliable oxidation reactions to synthesize fluorenol/fluorenone was only carried out at small scale and via non-green paths [9]. Many applications in industry for fluorenone/fluorenol compounds can be attained since they are used as basic materials in antimalaria drugs, insecticides, algaecides, biopharmaceutical dyes and as optical brightening agents [10]. In addition, some of their characteristics such as light and temperature sensitivities, heat resistance, conductivity and corrosion resistance make them applicable for use in the areas of thermo and light sensitizers, luminescence chemistry, spectrophotometric analysis and molecular chemistry [11,12]. The study of oxidation reactions is at the maximum of scientific activity. As a result, numerous methods have been developed to facilitate oxidation reactions particularly photocatalysis [13], which has recently grown as a technology provider. Photocatalysis opened new

* Corresponding author.
E-mail address: mohmok2000@yahoo.com (M.M. Mohamed).

http://dx.doi.org/10.1016/j.micromeso.2014.11.004
1387-1811/

approaches because it could be used under visible light irradiation and it also considered as a green method for synthesizing many organic compounds by substituting hazardous oxidizing compounds, of bad impact on the environment [14]. Correspondingly, investigations on alternative materials are uncommon. In this respect, bismuth oxide (Bi_2O_3) is an attractive material because of its good electrical conductivity and thermal properties. It is extensively used in various applications such as microelectronics, sensor technology and optical coatings [15,16]. As a photocatalyst, Bi_2O_3 is a p-type semiconductor with conduction and valence band edges +0.33 and +3.13 V relative to NHE, respectively. These values account for its capability to oxidize water and possibly generate highly reactive species, such as $O_2^{\cdot-}$ and $OH^{\cdot}$ radicals, which may act as initiators for oxidation reactions. On the other hand, SnO_2 is an important *n*-type wide-bandgap semiconductor with broad applications based on electrical and optical properties of the oxide, which also used as strong oxidation catalyst [17]. To the best of our knowledge, there are no reports on Pd doped SnO_2–Bi_2O_3. Such nanocomposites will have the potential to show the synergetic effect of Pd on the catalytic performance of the SnO_2–Bi_2O_3 catalyst towards partial oxidation of the fluorene pollutant. Many heterogeneous catalysts have been reported to be active for this transformation and recently supported Pd nanoparticles have been shown to be highly effective towards methyl orange degradation when supported on Bi_2O_3 [18]. With respect to palladium catalysis, it is known that this reactivity is due to small Pd nanoparticles and their interfaces with the supporting matrix are also important [8].

Accordingly, the aim of this study is to synthesize Bi_2O_3–SnO_2 composites with Bi/Sn atomic ratio of 3:1, loaded with Pd nanoparticles for fluorene partial oxidation; to fluorenol/fluorenone compounds, via using the photocatalysis approach. We employed UV–visible irradiations to create active species on the surface of the Bi_2O_3–SnO_2 catalysts to facilitate committing the oxidation processes at room temperature. This simple and low cost approach is a step forward towards tailoring photocatalysts for various purposes and it can valuably contribute to a photocatalyst design. The synthesized catalysts were thoroughly characterized using X-ray diffraction, Transmission electron microscope, UV–vis diffuse reflectance spectroscopy, N_2 sorptiometry and Raman-mapping spectrometry techniques.

2. Experimental section

2.1. Catalyst preparation

2.1.1. Synthesis of Pd/SnO_2–Bi_2O_3 nanostructures

All chemicals were analytical grade and used without further purification. In a typical procedure, appropriate amounts of $Bi(NO_3)_3{\cdot}5H_2O$ and $Sn(NO_3)_4$ were used so as to obtain a 3:1 atomic ratio in the final product. $Bi(NO_3)_3{\cdot}5H_2O$ was first dissolved in water containing polyethylene glycol-2000 [$(HO(CH_2CH_2O)_nH$)-PEG 2000-2 g/100 ml water)] (100 ml) and same for $Sn(NO_3)_4$. $Sn(NO_3)_4$ solution was poured onto the $Bi(NO_3)_3{\cdot}5H_2O$ solution under vigorous stirring. Ammonia solution (15%) was then added into the mixed solution in a drop wise manner until precipitation takes place and thus the reacting solutions were kept at 85 °C under vigorous stirring until a gel was formed. Then, the gel was transferred into a Teflon-lined stainless autoclave (300 mL capacity) at the temperature of 140 °C for 24 h via incubation in an electric oven. The system was then cooled to ambient temperature naturally. The as-prepared sample was collected and washed with distilled water and absolute ethanol several times, vacuum-dried and then calcined at 500 °C for 6 h to obtain SnO_2–Bi_2O_3 nanostructures. This sample was denoted as $SnBi3_{SG}$ where 3 accounts for the atomic ratio of 3/1(Bi/Sn) and SG is accounted for the sol–gel method of preparation. Palladium nitrate $Pd(NO_3)_2$ as to obtain a loading of 2% wt is taken as starting material to dope the $SnBi3_{SG}$ material, which has been dissolved in distilled water forming an emulsion using a ball mill. After mixing, PEG 6000 at a concentration of 3 g/100 ml was added step-wisely to the mixture for sake of Pd ions reduction. The mixture was left for one day under stirring, filtering and washing with distilled water for several times. Then, dried at 110 °C for 5 h and calcined at 500 °C for 6 h. This sample was denoted as Pd/$SnBi3_{SG}$.

2.1.2. Synthesis of Pd/Bi_2O_3 nanostructures

In a typical procedure, stoichiometric amounts of $Bi(NO_3)_3{\cdot}5H_2O$ was dissolved in 100 ml of distilled water containing polyethylene glycol-2000. The pH adjustment to a value of 8.8 via drop-wise addition of ammonia solution (15%, v/v) was performed until complete precipitation. After gelation for 24 h in a Teflon lined autoclave at 140 °C, the gel was then filtered, washed with distilled water for several times and dried at 110 °C over night. Finally, the sample was calcined at 500 °C for 6 h. To a portion of the calcined sample, an adequate amount of $Pd(NO_3)_2$ solution; so as to form a loading of 2% Pd, was added. Subsequently, vigorous stirring was achieved followed by drop-wise addition of PEG-6000 at a concentration of 3 g/100 ml. Calcinations at 500 °C for 6 h was accomplished following filtering, washing and drying at 110 °C. This sample was denoted as Pd/Bi_{SG}.

2.2. Catalyst characterization

2.2.1. X-ray diffraction

The X-ray powder diffraction patterns of various solids were carried out using a Philips 321/00 instrument. The patterns were run with Ni-filtered Cu Kα radiation ($\lambda = 1.541$ Å) at 36 kV and 16 mA with scanning speed of 2° in 2θ min^{-1}. The XRD phases present in the samples were identified with the help of ASTM powder data files.

2.2.2. N_2 adsorption

The surface properties namely BET surface area, total pore volume (V_p) and mean pore radius (r) were determined from N_2 adsorption isotherms measured at 77 K using conventional volumetric apparatus. The samples were out-gassed at 473 K for 3 h under a reduced pressure of 10^{-5} Torr before starting the measurement. The total pore volume was taken from the desorption branch of the isotherm at $p/p^0 = 0.98$, assuming complete pore saturation.

2.2.3. Ultraviolet–visible diffuse reflectance spectroscopy

Diffuse Reflectance Ultraviolet–visible spectroscopy (UV–vis DRS) of powder samples was carried out at room temperature using a PerkinElmer Lamda-900 spectrophotometer in the range of 200–800 nm. The UV–vis spectra were processed with Microsoft Excel software, consisting of calculation of the Kubelka–Monk function, $F(R_\infty)$, which was extracted from the UV–vis DRS absorbance. The edge energy (E_g) for allowed transitions was determined by finding the intercept of the straight line in the low-energy rise of the plot of $[F(R_\infty)hV]^2$, for the direct allowed transition, vs. hV, where hV is the incident photon energy.

2.2.4. Transmission electron microscope (TEM)

TEM micrographs were measured using a Philips; model Tecani Feil2, at an accelerating voltage of 200 KV. The powder samples were put on carbon foil with a microgrid. TEM images were observed with minimum electron irradiation to prevent damage to the sample structure. The elemental compositions of the composite material were investigated by energy-dispersive X-ray attached to the TEM equipment. The average particle diameter (d) was calculated by the following formula: $d = \Sigma nidi/\Sigma ni$, where

ni is the number of particle diameter di in a certain range, and Σni is more than 100 particles on TEM images of the sample. Computer-assisted counting of nanoparticle images and automated image analysis based software package including KONTRON KS 400 (Zeiss-Kontron) was used.

2.2.5. Raman spectroscopy

Raman spectroscopy was used to characterize the observed various phases. The LabRam HR is an integrated and compact Raman system. It is composed of a Helium Neon laser source, a confocal microscope coupled to a 800 mm focal length achromatic spectrograph and a two-dimensional multichannel CCD. The excitation wavelength of the internal 17 mW HeNe laser is 632.8 nm. An additional entrance for one or more external lasers is available in the basic version of the system. The integrated microscope is a high stability BX41 frame from Olympus. It incorporates white light both by reflection and by transmission. A video camera permits the user to control and to visualize the sample under the microscope objective and to check the position of the attenuated laser spot on this sample. The dispersive stage of the LabRAM HR is a Czerny-Turner achromatic spectrograph with a 30 mm wide flat field, optimized for a multichannel detection. This spectrograph is equipped with an automated twin grating turret offering high and low dispersion. The standard detector is a high performance TE cooled CCD detector of 1024 × 256 pixels (26 × 26 μm^2). The LabSpec software which controls the parameters of the system includes advanced treatment functions for Raman spectral analysis and imaging.

2.3. Measurements of photocatalytic activity

Fluorene (98%) used in the photooxidation experiments was used as received from Across. The photooxidation experiments were performed in a photoreactor made of quartz and equipped with a specific tubular space for the UV lamp as well as a cooling jacket. A high pressure Hg lamp (125 W) equipped with a UVA responsive to 320–400 nm; and presented strong emission lines at 325, 343, 365, 366 and 391 nm, manufactured by Vilber Lourmat, France was used as an UV light source; with an average light intensity equal 60 mW cm^{-2}. On the other hand, a Hg lamp (125 W) with a special UV cut off filter (λ = 420 nm) offering visible light source was also used. It was placed at a specified position using a special rod in the reactor. A continuous cold water (16 ± 1 °C) supply was maintained during the experiment to control the temperature of the reaction mixture. The 6x10^{-4} mol/l fluorene; dissolved in degassed acetonitrile solution, mixed with 100 mg of the photocatalyst was stirred for 30 min to prepare a uniform dispersion of the catalysts particles at room temperature followed by passage of an oxygen current through an inlet tube for 30 min at a 35 ml/min rate. After specified time, the oxygen current was ceased and the UV lamp was turned on. The experimental setup was completely covered with aluminum foil and samples were collected every hour for a period of 6 h for analysis using Shimadzu GC–MS-QP5050. This bench top quadrupole mass spectrometer features an extended mass range to 900 Daltons and optional positive and negative chemical ionization (PCI and NCI). Scan speeds of up to 6750 AMU/s were achieved with unit mass resolution. The MS was paired with GC-17A gas chromatograph, which uses Advanced Flow Control (AFC) for rapid as well as reproducible results. Ionization mode: EI, PCI, and NCI, Ionization voltage: 70 eV, Ionization current: 60 mA EI, 200 mA CI, Filament: dual, are implemented and well used. The % yield was calculated based on the amount of a particular product obtained from the reaction expressed in percentages. Quantifying the number of active surface sites on the metal oxide catalysts was done using the one common approach of employing O_2 chemisorption [19,20], which involves reducing the catalyst surface with H_2 and reoxidation to determine the number of active surface sites by the amount of O_2 adsorbed.

For detecting the active species [hydroxyl radicals (·OH), superoxide radical ($\cdot O_2^-$) and holes (h^+)] as well as their role in the photocatalytic reaction, the following scavengers were added: 1.0 mM isopropanol (IPA – a quencher of ·OH), p-benzoquinone (BQ – a quencher of $\cdot O_2^-$), and triethanolamine (TEOA – a quencher of h^+). The method was similar to the former photocatalytic experiments. As reported earlier the quantum yield [21] for the photooxidation process (ϕ_{ox}) was then determined as declared below. However, having a polychromatic radiation, quantum efficiency can be calculated on the bases of the total emission instead of adsorbed photons.

$$\Phi_{343} = \frac{\text{no. of molecules reacted}}{\text{no. of photons emitted}}$$

$$\text{No. of molecules reacted} = W/\text{Mol.wt} \times A \times \text{yield}$$

where A is Avogadro's number and W is the weight of certain product

$$\text{No. of photons emitted in 0.5 h(exposure time)} = \frac{\text{Total power emitted (amount of light emitted} \times \text{lamp power} \times \text{time/sec)}}{\text{Energy of single photon at 343 nm (hc/}\lambda\text{)}}$$

3. Results and discussion

3.1. XRD and TEM study

The XRD patterns of the as-prepared samples calcined at 500 °C are shown in Fig. 1. The pattern of SnO_2–Bi_2O_3 ($SnBi3_{SG}$) indicates various lines ascribed to Bi_2O_3 [at 2θ = 24.1°, 37.2° (104), 41° (120), 43.8° (113), 48° (202), 53.2° (024), 58.5° (116)], SnO_2 [at 2θ = 33.5° (101), 49.5° (211), 53.9° (220), 55.4° (002)] and $Bi_2Sn_2O_7$ [at 32.5°, 35° (331)] [22]. The XRD pattern of the Pd/$SnBi3_{SG}$ sample demonstrated apart from the existed lines ascribed to Bi_2O_3 [at 2θ = 24.1°, 48° (202), 53.2° (024)], the disappearance of some others related to the same species [at 2θ = 37.2° (104), 41° (120), 43.8° (113), 58.5° (116)]. New peaks at 2θ = 31.5° and 32.1° corresponding to the diffraction lines of (002) and (220) planes of the tetragonal β-Bi_2O_3 were also shown [23]. On the other hand, the recognized well crystallized SnO_2 lines

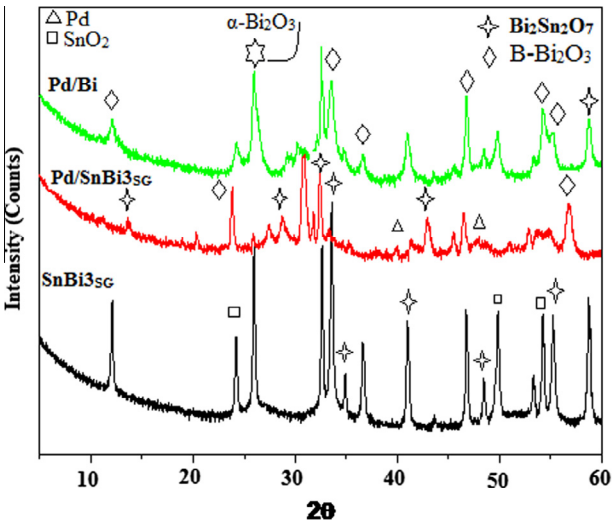

Fig. 1. XRD patterns of $SnBi3_{SG}$, Pd/Bi_{SG} and $Pd/SnBi3_{SG}$ obtained at room temperature.

shown in $SnBi3_{SG}$ were almost vanished in $Pd/SnBi3_{SG}$. Accordingly, the solubility of SnO_2 in Bi_2O_3 produces high $Bi_2Sn_2O_7$ concentration as confirmed by exposing typical peaks at $2\theta = 28.8°, 33.1°, 48.1°$and $57.5°$ [24] beside those mentioned before in the $SnBi3_{SG}$ sample and ascribed to the same phase. However, a marked decrease in crystallinity is indicated in the Pd containing sample as well as a peak broadening proposing a decrease in crystallites size of this particular sample comparatively. Accordingly, it can be suggested that $Bi_2Sn_2O_7$ was synthesized at the expense of SnO_2 vanishing. Of particular interest, the formation of the $Bi_2Sn_2O_7$ phase at such low temperature highlights the effect of template and hydrothermal conditions on the nucleation of this phase. The XRD pattern showed additional small intensity peaks at $2\theta = 40°$ and 47° ascribable to (111) and (200) planes of deposited Pd nanoparticles [25] as compared to the pattern of $SnBi3_{SG}$. These peaks are indexed to face-centered cubic Pd (Joint Committee on Powder Diffraction Standards (JCPDS) Card No. 05-0681, $a = 3.889$ Å). The XRD pattern of the as-prepared Pd/Bi_{SG} calcined at 500 °C using the precursors at the hydrothermal temperature of 140 °C is indexed to tetragonal crystallized β-Bi_2O_3 structure (PDF No. 27-50) with major peaks at $2\theta = 31.76°, 32.69°, 46.22°, 54.27°, 55.48°$ and $57.75°$ corresponding respectively, to the diffractions of (002), (220), (222), (203), (421) and (402). However, residual α-Bi_2O_3 was also appeared (PDF No. 6-294) with a major peak at $2\theta = 25.75°$ corresponding to the diffraction of the (002) plane of the monoclinic structure [26]. This proposes the stability of β-Bi_2O_3 over α-Bi_2O_3 following calcining at 500 °C. However, it has been acknowledged by many authors that metastable β-Bi_2O_3 changed gradually into α-Bi_2O_3 as the hydrothermal temperature increases [27]. This highlights that the adopted procedure is succeeded in obtaining a more stabilized phase for the former than that of the latter. A small peak due to Pd nanocrystallite was observed at $2\theta = 47°$ (200).

The morphologies of synthesized samples were examined by TEM. The TEM image of $SnBi3_{SG}$ shows irregular polygonal crystalline structure composed of tetragonal and hexagonal shapes with average sizes of 72 ± 1 nm (Fig. 2a). This image also shows an amorphous area with no agglomeration. The TEM image of $Pd/SnBi3_{SG}$ shown in Fig. 2b revealed a nanoplates-like structure with an average size of 44 ± 2 nm. The HRTEM image of the nanoparticles (seen as an inset) displayed resolved lattice fringes of 1.54 Å and 1.38 Å that indexed to (220) and (400) planes of β-Bi_2O_3 and $Bi_2Sn_2O_7$, respectively. This indicates the close proximity of crystallized β-Bi_2O_3 and $Bi_2Sn_2O_7$ phases. This close interconnection between the two phases is supposed to favor the photoinduced electrons transfer between the phases that assume to reduce the recombination of the photo-induced electrons and holes and improve the photocatalytic activity of the catalysts. The TEM image of Pd/Bi_{SG} (Fig. 2c) shows irregular crystalline nano-flake structure with average sizes of 20 ± 2 nm. Decreasing the particle size of this sample comparatively explains the role of the PEG template in slowing the nucleation rate via the sol–gel technique; compared with $Pd/SnBi3_{SG}$ that resulted in a

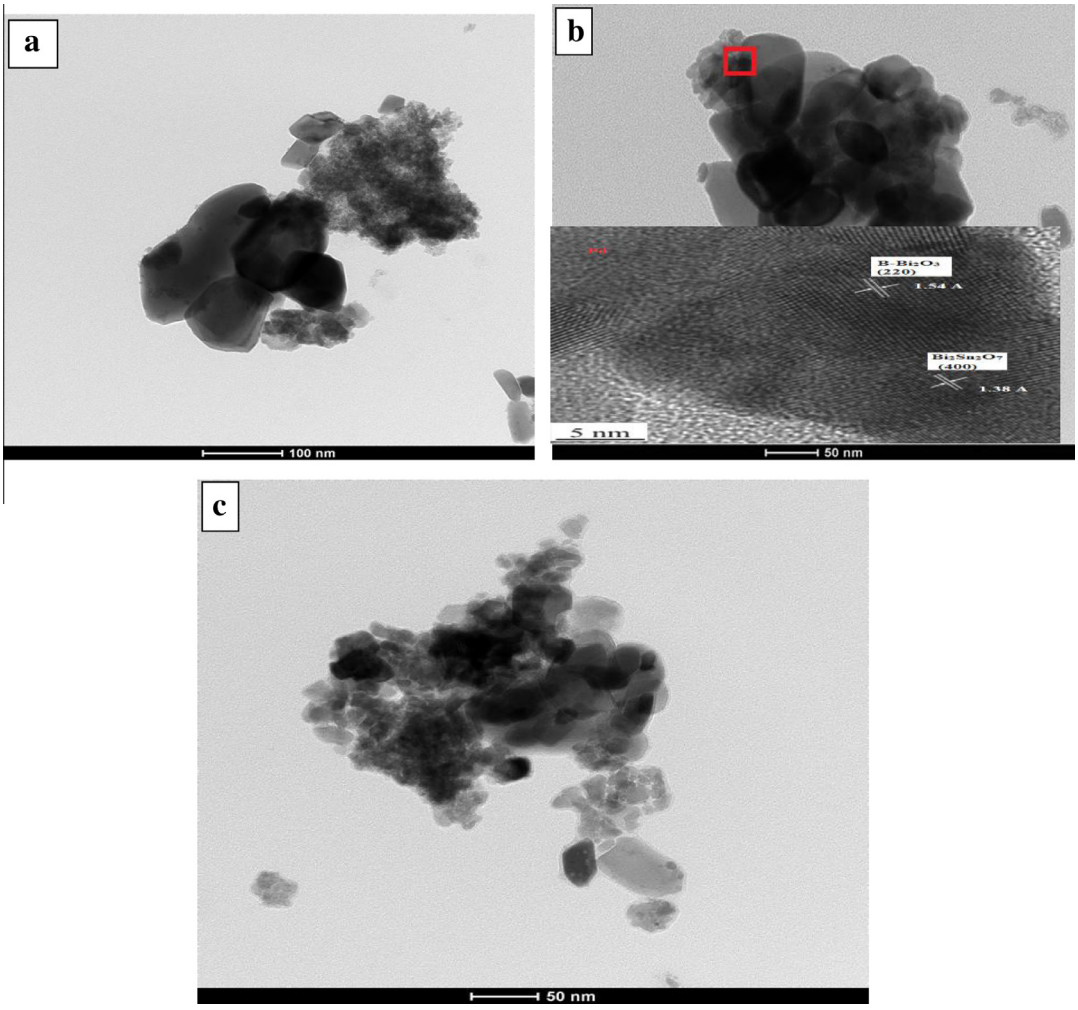

Fig. 2. (a) TEM image of $SnBi3_{SG}$, (b) TEM image of $Pd/SnBi3_{SG}$ and the inset figure is the magnification of the shaded red area together with elaborating Pd nanoparticles and (c) TEM image of Pd/Bi_{SG}. (For interpretation of the references to color in this figure legend, the reader is referred to the web version of this article.)

non-homogeneous nucleation so as to producing such irregular flaky structure.

3.2. Surface texturing

Full nitrogen sorption isotherms of synthesized samples were measured to obtain information about surface texturing properties (Fig. 3). A nearly linear correlation between the absorbed volume and relative pressure was observed in the relative pressure (P/P°) range of 0–0.6 and ascribed to unrestricted monolayer–multilayer adsorption. The sorption isotherms of the samples can be classified as type II, according to IUPAC classification and also exhibit H3-type hysteresis loops characteristic of mesoporous material consisting of slit-shaped capillaries. The large rise of nitrogen adsorption–desorption isotherms in the relative high pressure (P/P°) range of 0.8–1.0 was characteristic of mesoporous structure originated from the nanoporous walls or to the textural mesopores with quite assembled clusters [28]. The specific surface area of the $SnBi3_{SG}$ sample was calculated to be 20.8 $m^2\ g^{-1}$ as determined by the BET equation. The corresponding Barrett Joyner Halenda (BJH) analyses derived from the absorption branch of the isotherms exhibit that most of the pores fall into the size range from 2 to 50 nm. These pores presumably arise from the spaces among the oxides composite. However, the specific surface area of the $Pd/SnBi3_{SG}$ nanostructures was calculated to be 12 $m^2\ g^{-1}$, which is lower than that of Pd free sample proposing the inclusion of Pd nanoparticles deep inside the composite pores. As a confirmation, the desorption step in $Pd/SnBi3_{SG}$ was at $P/P^{\circ} = 0.73$ where it was at 0.6 for $SnBi3_{SG}$ reflecting the localization of Pd nanoparticles inside the pores and as a result the pore volume suffers a significant decrease (0.1564 cm^3/g-$Pd/SnBi3_{SG}$) when compared with the latter (0.2041 cm^3/g-$SnBi3_{SG}$). The $Pd/SnBi3_{SG}$ sample showed a trimodal distribution centered at 2.2 nm and 2.7 nm together with a broad one centered at 20 nm. On the other hand, the Pd/Bi_{SG} sample presented an average surface area of 21 $m^2\ g^{-1}$ with a bimodal pore size distribution centered at 3 nm and 10 nm revealing the existence of a shorter range of mesopores compared with the other two samples. All the samples presented similar adsorption–desorption isotherm except that narrowing parts of the mesoporous channels and creating ink-bottle like sections were discerned in the $Pd/SnBi3_{SG}$ sample as ascertained via involving trimodal distributions upon employing the PEG template. This could be due to depositing Pd and/or one of the oxides in the pore structure of the formed $SnBi3_{SG}$ phase; most probably SnO_2 as ascertained from XRD and thus creating such small distributions.

3.3. Optical properties

The optical absorption of synthesized nanostructures was measured by UV–vis diffuse reflection spectroscopy and the results

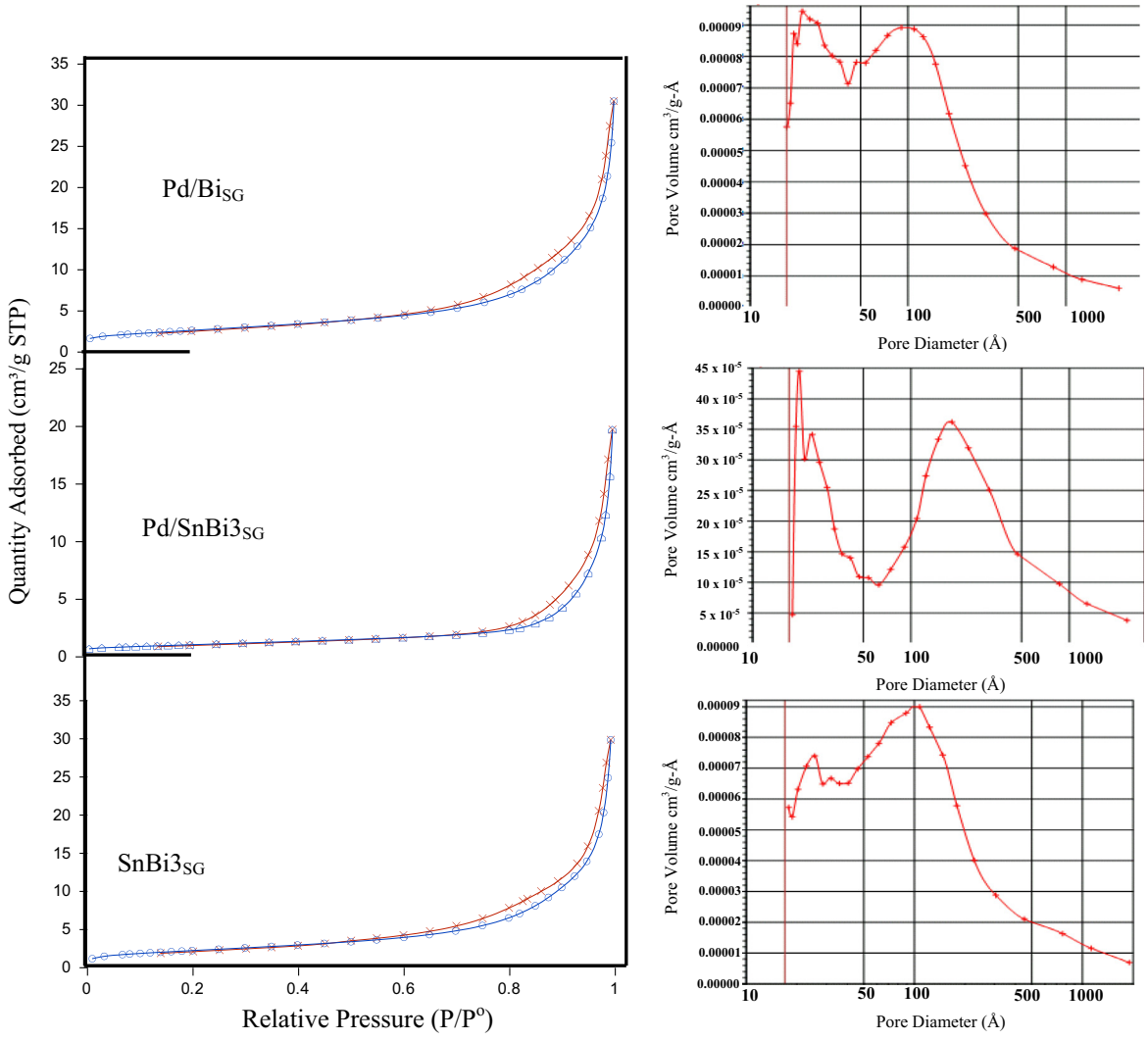

Fig. 3. Adsorption–desorption isotherms and the corresponding pore size distribution curves of $SnBi3_{SG}$, Pd/Bi_{SG} and $Pd/SnBi3_{SG}$.

were shown in Fig. 4. The absorbance edge of the as-prepared samples was located approximately in the wavelength range from 450 to 600 nm. A significant increase in the absorption at wavelengths shorter than 450 nm for $SnBi3_{SG}$ and Pd containing samples was assigned to the intrinsic band gap absorption of SnO_2 and Bi_2O_3 [29]. The sample Pd/Bi_{SG} has the strongest absorption probably due to surface roughness rather than due to increasing the particles size [30]. Conversely, this sample showed the lowest crystallites size as observed by TEM. The intensity of absorption was increased for Pd containing samples and even exhibited a red shift for the 337–350 nm band apart from the corresponding Pd free mixed oxide one ($SnBi3_{SG}$-325 nm). This proposes a decrease in their particles size as confirmed via XRD and TEM investigations.

The absorption edge of the former samples acquired an additional shift in the visible light region compared to $SnBi3_{SG}$. The band gap energies of the as-prepared $Pd/SnBi3_{SG}$ and Pd/Bi_{SG} were determined from the plot of $(ahv)^2$ vs. energy (hv) (the inset in Fig. 4) and were found to be at 2.10 and 2.0 eV, respectively. Whereas, the band gap of $SnBi3_{SG}$ heterostructures was found to be 2.4 eV. Such differences may be ascribed to the changes in crystalline phase and defects might be created following Pd incorporation [31]. Furthermore, transforming part of oxide phases; as depicted from XRD results, permanently from SnO_2 and Bi_2O_3 to $Bi_2Sn_2O_7$ could lead to a decrease in the band gap [29]. Optical characterization of nanocrystallites Bi_2O_3 and SnO_2 synthesized individually using some other methods indicate higher band gap values (2.85–2.8 eV) [32]. This highlights that the formation of $Bi_2Sn_2O_7$; based on the involvement of SnO_2 in the structure of Bi_2O_3, besides the adopted hydrothermal method could have a positive impact towards decreasing band gap values. On the other hand, no special surface Plasmon peak was noticed for Pd doped $SnBi3_{SG}$ and Bi (used to be at 390–420 nm) probably due to the well-dispersion of Pd nanoparticles; of low amount, and to the presence of isolated energy levels in the band gap of the semiconductor [33] composite. Accordingly, the peak at 410 nm cannot be assigned to surface Plasmon resonance of Pd nanoparticles since it appeared in the Pd free $SnBi3_{SG}$ sample.

3.4. Raman study

The spectra of the $SnBi3_{SG}$ material measured at 3 different positions presented fairly similar information (Fig. 5a). The Raman bands at 90 and 520 cm^{-1} are associated to the tetragonal phase of β-Bi_2O_3 whereas 146 and 210 cm^{-1} are due to monoclinic phase of α-Bi_2O_3 [34]. The new band at 390 cm^{-1}; which never seen in either tetragonal β or monoclinic α structures, could characterize the $Bi_2Sn_2O_7$ structure; in concordance with XRD results of

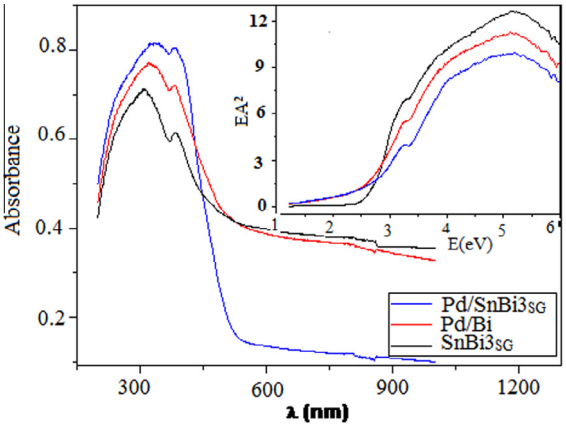

Fig. 4. UV–vis diffuse reflectance spectra of $SnBi3_{SG}$, Pd/Bi_{SG} and $Pd/SnBi3_{SG}$ and the inset is the corresponding Energy gap (E_g) values.

$SnBi3_{SG}$. To have a better overview of the homogeneity, an area of the sample was mapped (70 × 75 μm) (Fig. 5a1). Although all the spectra of the map are looking similar, small shifts in peak positions are observed at 146.9 and 147.9 cm^{-1} over the whole map. This slight difference is indicative to the sample heterogeneity. Accordingly, this might be due to slight changes in the particle size within the sample. It has been reported in the literature that Raman bands shift toward higher wavenumbers as the particle size decreases [35].

The Raman spectrum of Pd/Bi_{SG} measured at three different locations is depicted in Fig. 5b. For this sample, 3 factors are used to describe the dataset, each of them expressing some variation. In order to find out the different sources of variance in the map dataset, the MCR algorithm is applied. 3 MCR factors (or loadings) are used to describe the dataset; each individual spectrum of the map is a combination of the MCR factors altered by scores (coefficients where scores are displayed as maps). The first spectrum (A) presents peaks centered at 100 and 307 cm^{-1} assigned to the β-Bi_2O_3 (tetragonal) phase whereas that at 210 cm^{-1} is attributed to the α-Bi_2O_3 (monoclinic) phase [34]. The Raman peak of the higher frequency mode 210 cm^{-1} is attributed to the displacements of the O atoms in α-Bi_2O_3. Meanwhile, a strong peak is observed at 630 cm^{-1} together with a very small one at 735 cm^{-1}, corresponding to γ-Bi_2O_3 nanoparticles [36]. Mapping another area of the sample (B) indicates the intensity enhancement of the peaks assigned to β-Bi_2O_3 and α-Bi_2O_3 (100, 210 cm^{-1}) as well as the existence of a broad peak at 400 cm^{-1} due to β-Bi_2O_3 together with decrease in intensity of the peak positioned at 635 cm^{-1}. This indicates that the thermal treatment of Pd bismuth at 500 °C induces two effects: an oxidation followed by a structural transformation from the monoclinic α-Bi_2O_3 structure to major amounts of tetragonal β-Bi_2O_3 [37]. The significant Raman changes in the spectra are found in the spectrum map C; as for the strong peak appeared at 100 cm^{-1} due to β-Bi_2O_3 and the disappearance of the peaks correlated to γ-Bi_2O_3 and α-Bi_2O_3; in concordance with XRD results of this sample. Indeed, these obtained results measure the heterogeneity of the sample and the obvious increasing intensity ratio of β-Bi_2O_3, comparatively. This probably due to coating of the β-Bi_2O_3 phase and the increase of the disorder resulting from the hydrothermal reaction and Pd nanoparticles incorporation.

In order to find out the different sources of variance in the map dataset, the MCR algorithm is applied for the $Pd/SnBi3_{SG}$ sample (Fig. 5c). 4 MCR factors (or loadings) are used to describe the dataset; each individual spectrum of the map is a combination of the MCR factors altered by scores (coefficients). As observed in the Pd/Bi_{SG} sample, the different factors indicate the heterogeneity of the sample. Here, MCR factors 1 and 2 are looking similar; however all peaks are shifted of about 1–2 cm^{-1}, in a similar way as observed for the $SnBi3_{SG}$ sample (with potentially the same reasons explaining these shifts into slight chemical changes or particle size dependence). In this response, a doublet peak in the range 60–80 cm^{-1} together with small ones at 100 cm^{-1} and 150 cm^{-1} are discerned. These Raman phonons are associated to the tetragonal phase of β-Bi_2O_3 [38]. Some other broad modes are appeared at 255, 280, 405 and 540 cm^{-1}. They are assigned by comparison to infrared active modes to related pyrochlores [39–41] i.e. Raman active bands obtained for $Bi_2Sn_2O_7$. Accordingly, we assigned the modes observed at 255, 405 and 540 cm^{-1} due to the O–Sn–O bending, O motion in SnO_6 polyhedra (F_{2g}) and the O-vacancy stretching (A_{1g}), respectively. Whereas the peak at 280 cm^{-1} was due to α-Bi_2O_3 [42]. The latter modes together with that at 150 cm^{-1} were almost vanished in spectrum b due to sample heterogeneity. Factors 3 and 4 showed different features and express other source of variation within the dataset. They might not correspond to pure material spectra but account for some of the spectral

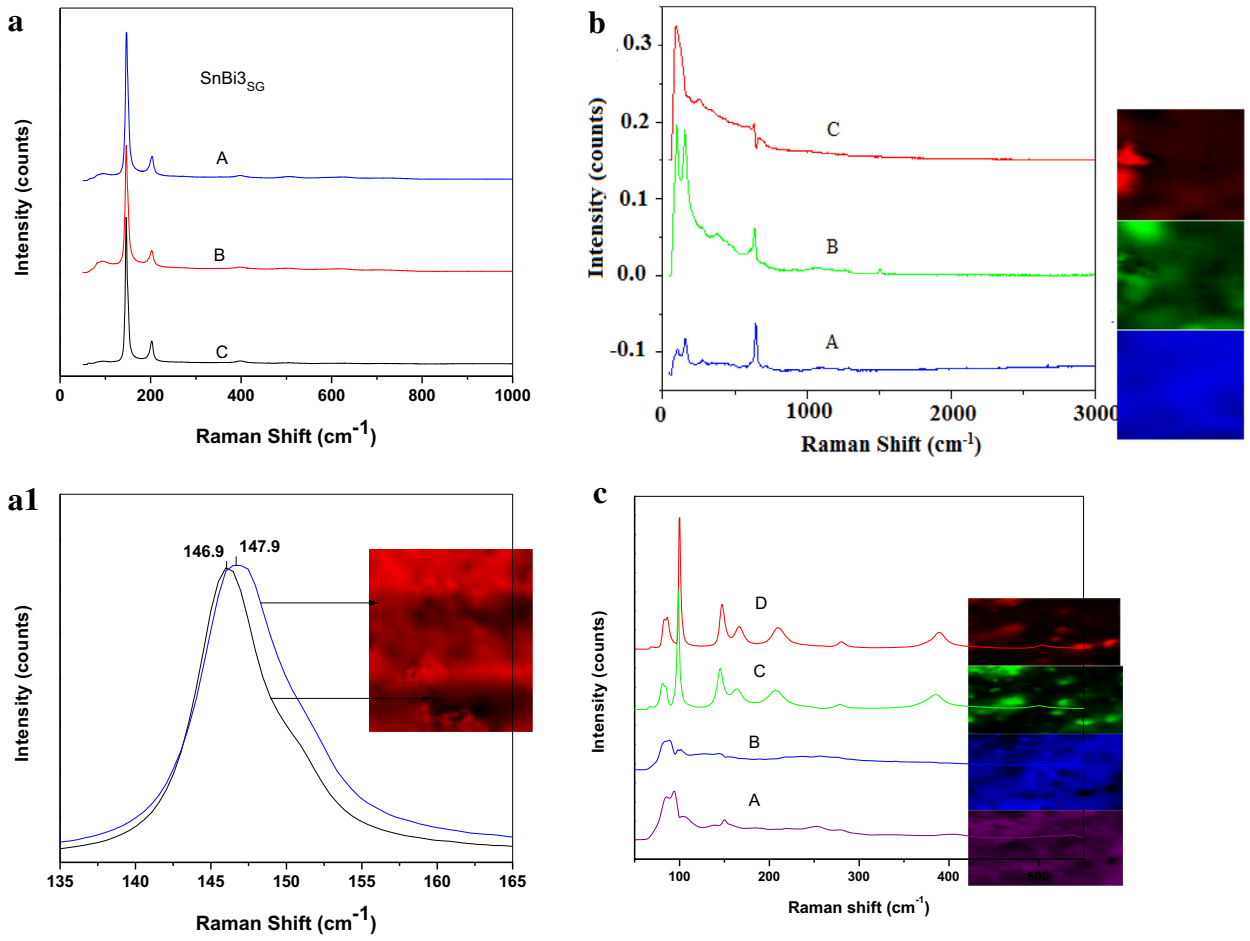

Fig. 5. (a) Raman spectra obtained for $SnBi3_{SG}$ at room temperature with vibration frequencies between 0 and 1000 cm^{-1} together with mapping spectra obtained in the 146–148 cm^{-1} margin (a1), (b) Raman and mapping spectra of Pd/Bi_{SG} with the vibration frequencies between 0 and 500 cm^{-1} and (c) Raman and mapping spectra of $Pd/SnBi3_{SG}$ with the vibration frequencies between 0 and 500 cm^{-1}.

variations of the map due to chemical and/or structural changes within the sample. Accordingly, spectra c and *d* almost show typical peaks at 65–75 cm^{-1} as doublet, 100s, 145, 170, 230, 274, 382 and 475 cm^{-1}. The Raman phonons observed till wavenumbers equal 100 cm^{-1} were typical of those seen in spectrum A. Raman phonons observed at 145 and 170 cm^{-1} were assigned to O–Bi–O bending (F_{1u}) and α-Bi_2O_3, respectively [43]. In the intermediate region, we assigned the modes observed at 274 and 382 cm^{-1} as being due to the O–Sn–O bending and Bi–O stretching. Similar to other pyrochlores, the (F_{2g}) was observed at lower wavenumbers than (E_g) mode in this region, thus we have assigned the 230 cm^{-1} modes as originating from the (F_{2g}) mode. The band observed at 475 cm^{-1} is assigned to the Sn–O stretching mode [44].

3.5. Photo-oxidation activity

3.5.1. Effect of different parameters on oxidation percentages

The effect of catalyst composition on fluorene photo-oxidation is illustrated in Fig. 6. It can be seen that $Pd/SnBi3_{SG}$ enhanced significantly fluorene percentages to 75% whereas Pd/Bi_{SG} verified a yield equal 62% after 6 h reaction time. On the other hand, the Pd free sample named $SnBi3_{SG}$ indicated lower activity comparatively and revealed a yield comprised of 35%, proposing that the active sites are due to the synergism between SnBi and Pd sites. A delay in the photo-oxidation of Pd/Bi_{SG}; up to 3 h, than $Pd/SnBi3_{SG}$ is due to the different in reactivity as the reaction proceed and this indeed is linked to the nature of active sites in the two catalysts

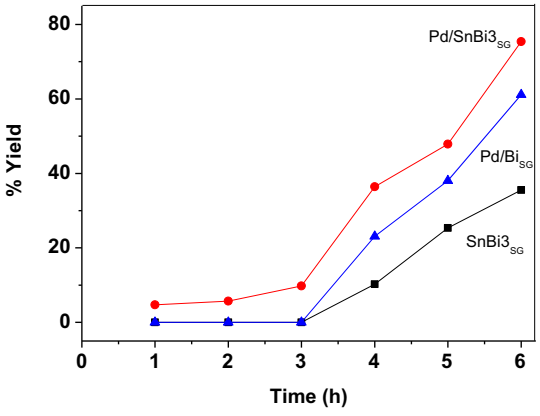

Fig. 6. Fluorene photooxidation (%) on $SnBi3_{SG}$, Pd/Bi_{SG} and $Pd/SnBi3_{SG}$ (reaction conditions: fluorene conc. = 6×10^{-4} mol/L, catalyst weight = 100 mg, time = 6 h, light intensity = 60 mW cm^{-2}, lamp power = 125 W). The O_2 flushing during illumination.

and how much time the reactant will stick to the surface to give product. Accordingly, we selected the $Pd/SnBi3_{SG}$ catalyst to perform some reactions to stand on the reasons of exceeding its activity. The effect of O_2 flushing either before or during irradiation was explored in Fig. 7. As it appears, flushing O_2 in advance before irradiation for 30 min shows 100% yield compared with that done

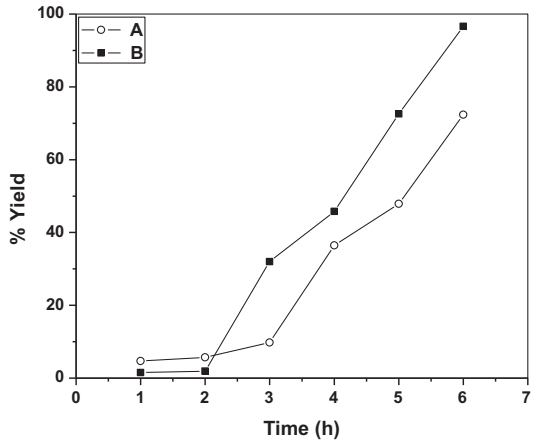

Fig. 7. Effect of O_2 flushing (A) during illumination and (B) prior to illumination (for 30 min) on the fluorene photo-oxidation activity of Pd/SnBi3$_{SG}$ (reaction conditions: fluorene conc. = 6×10^{-4} mol L^{-1}, catalyst weight = 200 mg, time = 6 h, light intensity = 60 mW cm^{-2}, lamp power = 125 W).

during irradiation and displayed a yield comprised of 70%. Additionally, an induction period of 2 h was observed in the former case, where it enlarged to 3 h in the latter one. Apparently, flushing O_2 prior to illumination stimulates the semiconductor composite to form O_2^- species; evidenced as one of the reactive species, resulted from capturing the conduction band electrons [45]. Indeed, these photogenerated superoxide radicals cause the oxidation of all fluorene present where in case of flushing during irradiation decreases the lifetime of oxidizing species; as depicted from longer induction period, and thus decreasing its power. Similarly, lowering the photo-oxidation yield of Pd/SnBi3$_{SG}$ following O_2 flushing prior to illumination (sample B) than for during illumination (sample A), in the first 2 h, is due to exposure of more O_2^- in the later than that in the former. However, Concurrent exposure to light and oxygen results in gradual surface oxidation and permeation of oxygen into the crystals at depths up to several hundred nanometers. This implies that oxygen can promote oxidation in several ways via stimulating the evolution of hydroperoxide formed via H abstraction; of lower mobility and oxidability as compared to O_2^-; from fluorene. The exposure of hydroperoxide moieties will indeed affect the oxidation of sample A after the induction period causing a marked decrease as in Fig. 7. On the other hand, the presence of excess amounts of oxidizing species in the latter case can also oxidize the semiconductors (Sn Bi; p–n junction) into higher oxidation states by which an increase in band gap can be obtained [46]. Although Pd/Bi$_{SG}$ presented slightly lower band gap energy and increased surface area values (2.0 eV and 20.8 m^2/g) than Pd/SnBi3$_{SG}$ (2.1 eV and 12 m^2/g), it presented lower activity. This was in part due to the facile transfer of electrons from β-Bi_2O_3 to $Bi_2Sn_2O_7$; in Pd/SnBi3$_{SG}$, due to their close contact as evidenced from TEM results and thus hindering charges recombination. Besides, the surface roughness depicted in Pd/Bi$_{SG}$ affected the absorption; as illustrated in TEM results and confirmed via UV–vis diffuse reflectance findings, and thus undergoing into enough emission for stimulating electron-hole production was slightly ceased. No one can deny the influence of SnO_2 in the photo-oxidation process of Pd/SnBi3$_{SG}$ decisively in leading to the formation of $Bi_2Sn_2O_7$ that played a unique role in the reaction. Indeed, Raman spectra confirmed the latter result and indicated the existence of the chemical bond O–Sn–O within the bulk structure of Bi_2O_3. Additionally, based on the results obtained from N_2 sorptiometry, this sample was particularly affected by high margin of mesopore sizes rather than surface area value. On the other hand, although the sample SnBi3$_{SG}$ presented all the phases, including Bi_2O_3, SnO_2 and $Bi_2Sn_2O_7$, it presented the lowest activity probably because of exposing SnO_2 species, the absence of Pd nanoparticles as well as increasing the average particle size (72 nm) than rest of the samples. Indeed, this assures the ability of Pd nanoparticles towards oxidation reactions and emphasizes as well its ability to direct the introduction of a new functionality in a great number of processes including hydrogenations and C–C couplings [47,48]. From the electronic transitions as well as compositional point of views it was depicted via Raman that the most prominent phase was the tetragonal β-Bi_2O_3 in all samples that constituted with the $Bi_2Sn_2O_7$ phase the most active sites for the reaction; as clarified in Pd/SnBi3$_{SG}$. However, there is an uncertainty for the α-Bi_2O_3 phase; which hardly detected in the Raman spectra of Pd/SnBi3$_{SG}$. On the other hand, although Raman provoked the existence of γ-Bi_2O_3 phase; which never detected in XRD probably for high dispersion and decreased crystallite size and concentration, its share in the oxidation reaction is doubtful since it is never seen in Pd/SnBi3$_{SG}$ that presented the highest activity. Exposing the synthesized materials to visible light irradiation under the conditions stated in Fig. 6 indicate 72%, 86% and 20% yield for Pd/Bi$_{SG}$, Pd/SnBi3$_{SG}$ and SnBi3$_{SG}$, respectively reflecting that the nanocomposite photocatalyst Pd/SnBi3$_{SG}$ has a good sensitizer harvesting visible light capabilities. Indeed, this result indicates that constructing Pd nanoparticles on the surface of SnBi3$_{SG}$ makes this catalyst an efficient photocatalyst.

The effect of catalyst amount on the photocatalytic activity was then studied using three different suspensions of Pd/SnBi3$_{SG}$ (Fig. 8). We observed that the increase in the amount of the catalyst into 200 mg in the reaction mixture causes an increase in the % yield into 100 in only 5 h. Reaching to that maximum value of the reaction yield indicates the absence of shadow effects at that concentration (200 mg). On the other hand, the decrease in yield at 100 mg catalyst into 40% reflects the decrease in the reactive oxidizing species at that concentration. Contrarily, a marked decline in the oxidation products into 20% yield was attained as the catalyst loading increased up to 300 mg. The presence of an optimum in photocatalyst concentration is quite common in this type of processes and is normally related to the potential shielding effect made by an excess of solids towards the penetrating radiation. It was observed that the fraction of fluorene adsorbed prior to illumination stage was significantly small comprised of 10% as determined via spectrophotometric analysis. They comprised of 5.9×10^{-5} mol/0.1 g and 11.7×10^{-5} mol/0.2 g for 100 and 200 mg, respectively.

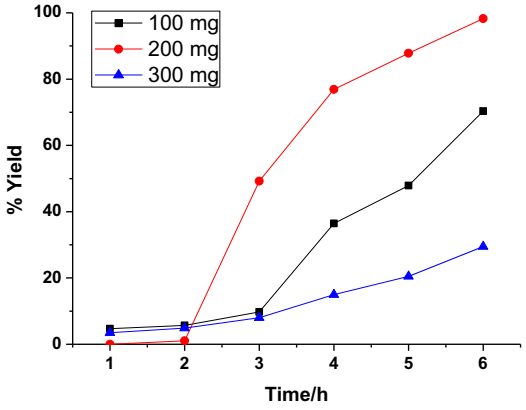

Fig. 8. Effect of catalyst weight on fluorene photo-oxidation activity of Pd/SnBi3$_{SG}$ (reaction conditions: fluorene conc. = 6×10^{-4} mol L^{-1}, time = 6 h, catalyst weight = 200 mg, light intensity = 60 mW cm^{-2}, lamp power = 125 W, O_2 flushing before illumination at 35 ml/min for 30 min).

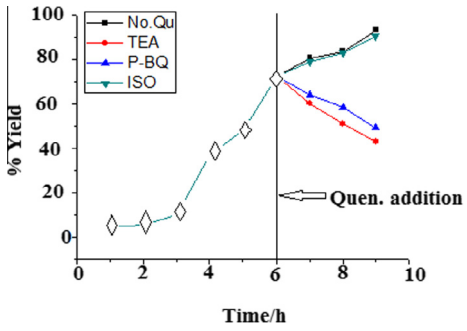

Fig. 9. Effect of reactive intermediates (isopropanol, IPA; p-benzoquinone, BQ; triethanolamine, TEOA) on the activity of Pd/SnBi3$_{SG}$ towards fluorene photo-oxidation (reaction conditions: fluorene conc. = 6×10^{-4} mol L^{-1}, time = 6 h, catalyst weight = 200 mg, light intensity = 60 mW cm^{-2}, lamp power = 125 W, O_2 flushing during illumination at 35 ml/min for 30 min).

3.5.2. Effect of different scavengers and identification of oxidation products

The effect of scavenging agents such as isopropanol (IPA – a quencher of ·OH), p-benzoquinone (BQ – a quencher of $\cdot O_2^-$), and triethanolamine (TEOA – a quencher of h^+) towards the photo-oxidation of fluorene was investigated under optimum conditions to investigate the active species which might exist in the photo-oxidation process [49]. As shown in Fig. 9, the presence of BQ and TEA scavengers lowered significantly the rate of the photo-oxidation activity in the system. Accordingly, this revealed that holes and O_2^- moieties are the reactive species in the photo-oxidation reaction than that of ·OH species.

The photolysis of fluorene under UV-A radiation did not show any appreciable oxidation products or elimination of the parent compound. Fluorene gave two main product peaks under our analytical condition upon using the Pd/SnBi3$_{SG}$ photocatalyst. The components of the peaks were identified as fluorenone and fluorenol as determined by the spectral database of GC/MS. The obtained data showed that fluorenone was the major product (~74%) whereas fluorenol was the minor one (~25%) accompanied with minute amounts of phthalic anhydride and dibenzofuran (see Table 1). In case of Pd/Bi$_{SG}$, the same components were formed but at lower yield comprised of 45.35% fluorenone and 20.56% fluorenol together with appreciable amounts of phthalic anhydride and dibenzofuran exceeding those delivered using the former photocatalyst. It seems also that the composition of composites plays a significant role on the selectivity towards the products. Based on the obtained results, one can assume that increasing fluorenone/fluorenol ratio was dependant on $Bi_2Sn_2O_7$ and β-Bi_2O_3 heterostructures beside Pd nanoparticles. However, the decrease in this ratio as evidenced in Pd/Bi$_{SG}$ can be correlated to the absence of $Bi_2Sn_2O_7$ as well as to the decrease in the concentration of β-Bi_2O_3 in favor of α-Bi_2O_3. On the other hand, the SnBi3$_{SG}$ sample indicated the lowest yield comparatively (60%) and produced the least values of fluorenone (31.26%) and fluorenol (12.73%) (Table 1). As a confirmation, the TOF value of the latter sample decreases compared to the rest of samples (Table 1). Although Pd/Bi$_{SG}$ and Pd/SnBi3$_{SG}$ presented equal conversion and TOF values they displayed different selectivities. Therefore, the intrinsic activity follows a different trend. Based on the obtained results, this could probably explain the importance of $Bi_2Sn_2O_7$/β-Bi_2O_3 heterostructures as well as the mesoporosity significance of Pd/SnBi3$_{SG}$ rather than the size of crystallites that was lower in the Pd/Bi$_{SG}$ sample. Furthermore, enhancing the adsorption initially on the later catalyst could also share on varying the selectivity ratios. Furthermore, it was confirmed that the fluorenone formed by the oxidation of fluorene is very stable under light irradiation.

Light absorption of energy equal to or greater than the band gap energy of Pd/SnBi3$_{SG}$ (i.e. 2.1 eV) will result in electron ejection from the valence band to the conduction band generating a reactive electron and a positive hole: Pd/SnBi3$_{SG}$ + $h\nu$ → Pd/SnBi3$_{SG}$ (e^-_{CB} + h^+_{VB}). Accordingly, the electron–hole generation can be proposed to describe the resulting compounds in Table 1 and Scheme 1. The photogenerated electron can be trapped by adsorbed oxygen to form superoxide or other negatively charged adsorbed oxygen species: $O_2 + e^-_{CB} \rightarrow O_2^-$. As the oxidizing power of the hole (+2.4 V vs. SCE in acetonitrile) is capable of initiating single electron oxidation of an adsorbed fluorene, the fluorene radical cation can be formed which rapidly deprotonated to fluorene-hydroxy radical. The radical intermediate is easily oxidized with the photogenerated superoxide or even with oxygen to give fluorenone/fluorenol products, as illustrated in Scheme 1. Accordingly, photocatalytic oxidation of fluorene methylene group to dibenzofuran/phthalic anhydride formation via reaction with the superoxide or with oxygen can be suggested [50]. The same mechanism was recommended by Liang and Liu [51] accounted for photocatalytic oxidation of diphenyl methane and by Fox et al. [52] in the case of naphthalenes. To prove that this reaction was initiated by a radical mechanism; based on the formation of O_2^-, rather than singlet oxygen ($^1O_2$); that expected to be generated under similar conditions, a tetraphenylporphyrin sensitizer [21] was used. The results indicate that the photooxidation was not affected accomplishing that free singlet oxygen plays no role in the current photo-oxidation reaction.

3.5.3. Quantum yield study

Values of quantum yield Φ for similar fluorene concentrations, oxygen content of the solvent and its dependence on amount of photons emitted at specific wavelength are presented in Table 1. As can be seen from the data in Table 1, the quantum yield of the photo-oxidation of Pd/SnBi3$_{SG}$ is increased (0.1 ± 0.05) and exhibited a straightforward photochemical dependant reaction, including at least one possible mechanism. This may be associated with an electron transfer process proceeding from the composite to adsorbed O_2 forming $\cdot O_2^-$. On the other hand, the hole is able to initiate single electron oxidation of fluorene forming a radical cation; as mentioned previously. This mechanism is nearly dependent on the oxygen concentration (that was kept constant) and is characterized by an increase in Φ under short wavelength excitation.

Table 1
The percentage of the products with the synthesized photocatalysts and quantum yields calculation.

Catalyst	Conversion %	TOF[a] × 10^{-6} s^{-1}	Quantum[b] yield	Product fluorenone	Selectivity fluorenol	% Dibenzofuran	Phthalic anhydride
Pd/Bi$_{SG}$	100(72)	9.4	0.03	55.35	23.56	7.20	5.80
Pd/SnBi3$_{SG}$	100(86)	9.4	0.1 ± 0.05	73.95	24.77	0.64	0.64
SnBi3$_{SG}$	60(20)	3.3	10^{-2}	31.26	12.73	9.51	6.5

Values in parentheses are for conversion % values obtained after exposure to visible light irradiation.
Conversion % measures of the moles reacted/feed moles × 100.
[a] TOF = TON/time (s) where TON = mol of products/mol of catalyst (support).
[b] Quantum yields were calculated based on const. fluorene conc., const. O_2 flushing amount as well as time and at specific wavelength and on only varied photon emitted amount for every catalyst.

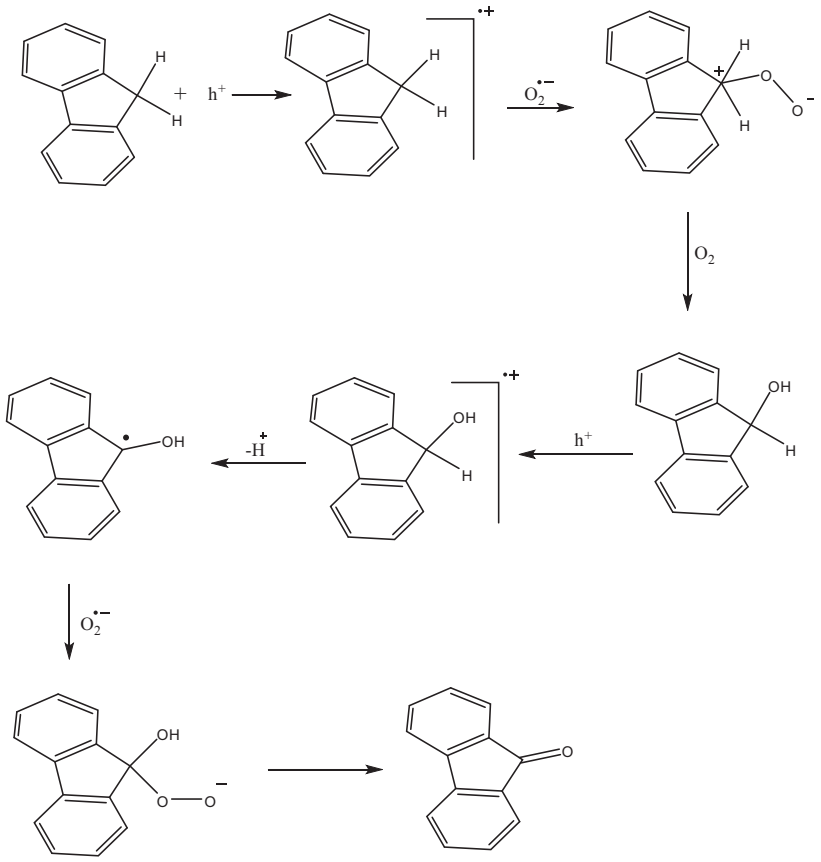

Scheme 1. Proposed mechanism for the photocatalytic oxidation of fluorene.

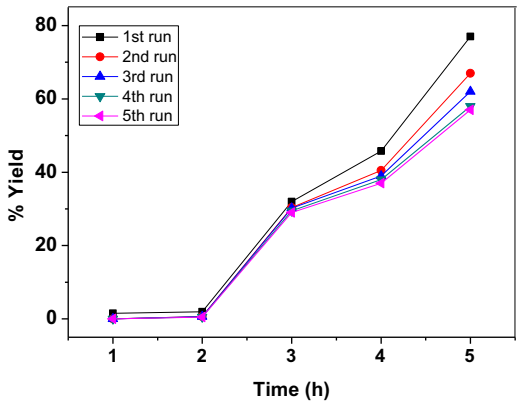

Fig. 10. Reusability of Pd/SnBi3$_{SG}$ on fluorene photo-oxidation activity (reaction conditions: fluorene conc. = 6 × 10^{-4} mol L^{-1}, time = 6 h, catalyst weight = 100 mg, light intensity = 60 mW cm^{-2}, lamp power = 125 W, O_2 flushing before illumination at 35 ml/min for 30 min).

The values of Φ for Pd/SnBi3$_{SG}$ showed a decrease into 0.03 for Pd/Bi$_{SG}$ and 10^{-2} for SnBi3$_{SG}$. This highlights the weak dependence of the photo-oxidation reaction on the quantum yields of latter catalysts specifically Pd/Bi$_{SG}$; that showed comparable activity (similar TOF values) to Pd/SnBi3$_{SG}$. This proposes that there are different dominant roles other than quantum yield affecting on the photo-oxidation of the former.

3.5.4. Influence of catalyst reuse

One of the economic vital factors in catalytic processes is the stability of the catalyst. In the present work this factor was measured by completing several consecutive experiments with the same catalyst and under uniform operating conditions (Fig. 10). A direct comparison of the yield obtained when fresh catalyst was used and after five reuses shows that the differences are minimal, indicating that the catalyst has mostly recovered its photo-oxidation activity. A plot of % yield for runs completed with reused catalyst versus time gives an activity comprised of 68.8% after 25 h. From the previous results, it can be hypothesized that fluorene has been well oxidized on the Pd/SnBi3$_{SG}$ photocatalyst. It has been acknowledged that the adsorption capacity of the previous catalyst remains unchanged, likely the intermediates formed after fluorene oxidation are also oxidized or desorbed into the aqueous bulk as oxidized moieties.

4. Conclusions

Novel hetero-junction $Bi_2Sn_2O_7$/β-Bi_2O_3; synthesized using the sol–gel and PEG template, loaded Pd presented superior photocatalytic performances towards fluorene partial oxidation (100% yield) into fluorenone/fluorenol products. This improved photocatalytic performance was basically attributed to the electron transfer across the hetero-structure $Bi_2Sn_2O_7$/β-Bi_2O_3, to the modified electronic structure of Pd and its dispersion in SnBi3$_{SG}$ as well as to the high quantum yield value. The effects of catalyst composition, catalyst weight percentages, O_2 flushing and reactive species scavengers have been evaluated. An electron–hole pair generated on the irradiated Pd/SnBi3$_{SG}$ surface was suggested for the semiconductor-mediated photocatalysis rather than singlet oxygen mechanism. Raman-mapping gives an idea about chemical differences or particle size dependences via comparison and it was well integrated with XRD, TEM and UV–vis diffuse reflectance techniques

to obtain well correlation and enriched deep information. Appreciable activities were also depicted following visible light irradiation and provided some useful guide lines for the rational design of visible light photocatalysts. The Pd(0) can play an important role in the charge separation, and serve as reactive sites for oxygen reduction to scavenge the excited electrons, thereby improving the photocatalytic performance in combination with the strong oxidizing power of holes and O_2^- moieties.

Acknowledgment

We thank the HORIBA Jobin Yvon SAS laboratories for their help in performing Raman analysis.

References

[1] O. Gimeno, F.J. Rivas, F.J. Beltrán, M. Carbajo, Chemosphere 69 (2007) 595–604.
[2] J.P. Buchet, J.P. Gennart, F. Mercado-Calderon, J.P. Delavignette, L. Cupers, R. Lauwerys, Br. J. Ind. Med. 49 (1992) 61–768.
[3] M. Baerns, H. Borchert, R. Kalthoff, P. KaDner, F. Majunke, S. Trautmann, A. Zein, P. Ruiz, B. Delmon (Eds.), Catalysis Studies in Surface Science and Catalysis, vol. 12, Springer, 1982, pp. 51–60.
[4] J. Bünger, J. Krahl, A. Weigel, O. Schröder, T. Brüning, M. Müller, E. Hallier, G. Wesphal, Arch. Toxicol. 80 (2006) 540–546.
[5] J. Sabate, J.M. Bayona, A.M. Solanas, Chemosphere 44 (2001) 119–124.
[6] D.B. Kittelson, J. Aerosol Sci. 29 (1998) 575–588.
[7] H.T. Yu, J. Environ. Sci. Health C Environ. Carcinog. Ecotoxicol. Rev. 20 (2002) 149–183;
Y.C. Lin, W.J. Lee, H.C. Hou, Atmos. Environ. 40 (2006) 3930–3940.
[8] L. Liu, B. Yang, H. Zhang, S. Tang, Z. Xie, H. Wang, Z. Wang, P. Lu, Y. Ma, J. Phys. Chem. C 112 (2008) 0273–10278.
[9] S.M. Correa, G. Arbilla, Atmos. Environ. 40 (2006) 6821–6826.
[10] D. Dunn, G. Hostetler, M. Iqbal, V.R. Marcy, Y.G. Lin, B. Jones, L.D. Aimone, J. Gruner, M.A. Ator, E.R. Bacon, S. Chatterjee, Bioorg. Med. Chem. Lett. 22 (11) (2012) 3751–3753.
[11] T.A.M. Ferenczi, M. Sims, D.D.C. Bradley, J. Phys.: Condens. Matter 20 (4) (2008) 045220–045224.
[12] L. Feng, C. Zhang, H. Bie, Z. Chen, Dyes Pigm. 64 (2005) 31–40.
[13] M.M. Mohamed, S.A. Ahmed, K.S. Khairou, Appl. Catal. B Environ. 150- 151 (2014) 63–73.
[14] N.T. Vandenborre, E. Husson, H. Brusset, Spectrochim. Acta A 37 (1981) 113.
[15] W.D. He, W. Qin, X.H. Wu, X.B. Ding, L. Chen, Z.H. Jiang, Thin Solid Films 515 (2007) 5362–5365.
[16] S.J.A. Moniz, D. Bhachu, C.S. Blackman, A.J. Cross, S. Elouali, D. Pugh, R.Q. Cabrera, S. Vallejos, Inorg. Chim. Acta 380 (2012) 328–335.
[17] N. Van Hieu, L.T.B. Thuy, N.D. Chien, Sens. Actuators B 129 (2008) 888–895.
[18] J. Zhong, J. Li, F. Feng, G. Fan, J. Zeng, S. Huang, W. Hu, M. Li, Environ. Prog. Sustain. Energy (2014), http://dx.doi.org/10.1002/ep.11919.
[19] A.N. Desikan, L. Huang, S.T. Oyama, J. Phys. Chem. 95 (1991) 10050–10056.
[20] K.V.R. Chary, V. Vijayakuma, P.K. Rao, Langmuir 6 (1990) 1549–1554.
[21] P.D. Bartlett, M.E. Landis, J. Am. Chem. Soc. 99:9 (1977) 3033–3037.
[22] A. Montenegro, M. Ponce, M.S. Castro, J.E. Rodŕıguez-Paez, J. Eur. Ceram. Soc. 27 (2007) 4143–4146;
H.W. Kim, S.H. Shim, J.W. Lee, J.Y. Park, S.S. Kim, Chem. Phys. Lett. 456 (2008) 193–197.
[23] L. Bourja, B. Bakiz, A. Benlhachemi, M. Ezahri, J.C. Valmalette, S. Villain, J.R. Gavarri, J. Taibah Univ. Sci. 4 (2010) 1–8.
[24] D.-W. Yuan, R.-F. Yan, G. Simkovich, J. Mater. Sci. 34 (1999) 2911–2918.
[25] R. Nie, J. Shi, W. Du, Z. Hou, Appl. Catal. A 473 (2014) 1–6.
[26] J.-y. Xia, M.-t. Tang, C. Cui, S.-m. Jin, Y.-m. Chen, Trans. Nonferrous Met. Soc. China 22 (2012) 2289–2294.
[27] T.-C. Kuo, Y.-L. Kuo, W.-C.J. Wei, J. Eur. Ceram. Soc. 31 (2011) 3153–3158.
[28] M.M. Mohamed, M.S. Al-Sharif, Appl. Catal. B 142- 143 (2013) 432–441.
[29] A. Hameed, T. Montini, V. Gombac, P. Fornasiero, J. Am. Chem. Soc. 130 (2008) 9658–9659.
[30] J. Wu, F. Huang, X. Lü, P. Chen, D. Wan, F. Xu, J. Mater. Chem. 21 (2011) 3872–3876.
[31] L. Zhang, W. Wang, J. Yang, Z. Chen, W. Zhang, L. Zhou, S. Liu, Appl. Catal. A 308 (2006) 105–110.
[32] F. Pourfayaz, A. Khodadadi, Y. Mortazavi, S.S. Mohajerzadeh, Sens. Actuators B 108 (2005) 72–179.
[33] P. Maruthamuthu, M. Ashokkumar, Sol. Energy Mater. 17 (1988) 433–439.
[34] S.N. Narang, N.D. Patel, V.B. Kartha, J. Mol. Struct. 327 (1994) 221–227.
[35] D.H. Franklin, I.E. Wachs, J. Solid State Chem. 97 (1992) 319–325.
[36] S. Venugopalan, A.K. Ramdas, Phys. Rev. B 5 (1972) 4065–4069.
[37] J. Cheng, H. Xin, H. Zheng, B. Wang, J. Power Sources 232 (2013) 152–158.
[38] D.J. Arenas, L.V. Gasparov, W. Qiu, J.C. Nino, C.H. Patterson, D.B. Tanner, Phys. Rev. B 82 (2010) 214302–214308.
[39] M.H. Chen, D.B. Tanner, J.C. Nino, Phys. Rev. B 72 (2005) 54303–54309.
[40] H. Wang, S.R. Foltyn, Q.X. Jia, P.N. Arendt, X. Zhang, J. Appl. Phys. 100 (2006) 053904–053909.
[41] M. Fischer, T. Malcherek, U. Bismayer, P. Blaha, K. Schwarz, Phys. Rev. B 78 (2008) 014108–014112.
[42] S. Brown, H.C. Gupta, J.A. Alonso, M.J. Martinez-Lope, Phys. Rev. B 69 (2004) 054434–054439.
[43] H.C. Gupta, S. Brown, N. Rani, V.B. Gohel, Int. J. Inorg. Mater. 3 (2001) 983–990.
[44] M. Maczka, J. Hanuza, K. Hermanowicz, A.F. Fuentes, K. Matsuhira, Z. Hiroi, J. Raman Spectrosc. 39 (2008) 537–544.
[45] L. Liu, S. Tang, M. Liu, Z. Xie, W. Zhang, P. Lu, M. Hanif, Y. Ma, J. Phys. Chem. B 110 (2006) 13734–13740.
[46] H.W. Kim, S.H. Shim, J.W. Lee, J.Y. Park, S.S. Kim, Chem. Phys. Lett. 456 (2008) 193–197.
[47] M.M. Ibrahim, S.A. Ahmed, K.S. Khairou, M.M. Mohamed, Appl. Catal. A 475 (2014) 90–97.
[48] O.S. Mohamed, J. Photochem. Photobiol. A Chem. 152 (2002) 229–232.
[49] D. Astruc, F. Lu, J.R. Aranzaes, Angew. Chem. Int. Ed. 44 (2005) 7852–7872.
[50] J. Durand, E. Teuma, M. Gomez, Eur. J. Inorg. Chem. (2008) 3577–3586.
[51] J.-J. Liang, T.-J. Liu, J. Chin. Chem. Soc. 32 (1986) 133–139.
[52] M.A. Fox, C.C. Chen, J.N.N. Yonnathan, J. Org. Chem. 40 (1984) 1969–1975.